Available online at www.sciencedirect.com
ScienceDirect
Comput. Methods Appl. Mech. Engrg. 294 (2015) 56–71
Computer methods in applied mechanics and engineering
www.elsevier.com/locate/cma

Multiwavelet discontinuous Galerkin *h*-adaptive shallow water model

Georges Kesserwani[a,b], Daniel Caviedes-Voullième[a,b,*], Nils Gerhard[b], Siegfried Müller[b]

[a] *Civil & Structural Engineering, University of Sheffield, Sheffield, UK*
[b] *Institut für Geometrie und Praktische Mathematik, RWTH Aachen, Templergraben 55, D52056, Aachen, Germany*

Received 29 July 2014; received in revised form 13 April 2015; accepted 27 May 2015
Available online 4 June 2015

Abstract

This paper presents a Godunov-type numerical formulation that is local, conservative and scalable in both accuracy and resolution. The keystone of the framework is to recast a *local* multi-resolution *discontinuous Galerkin* formulation and, combine it with *multiwavelets* (*MWDG*) to adaptively determine local resolution level by manipulating multiwavelet coefficients driven by one threshold value set by the user. Recent advances in discontinuous Galerkin modelling of the shallow water equations with topography source term are directly transferred to the MWDG framework. The adaptive MWDG model is tested for simulation of transient and steady shallow flow test cases demonstrating ability to model compound flows with appropriate level resolutions, and with comparable predictive quality as uniform mesh counterpart corresponding to highest resolution available.

Keywords: Resolution adaptability; Discontinuous Galerkin; Multiwavelets; Shallow water flow

1. Introduction

Shallow water modelling is central to the field of Computational Hydraulics, in which Godunov-type numerical methods have become far-reaching [1]. The class of Godunov-type numerical methods excels in a distinctive conceptual formulation that comprehensively incorporates solution discontinuities and forms the basis of the latest flood modelling tools for simulating the widest range of flow transitions [2–4].

The philosophy underlying a Godunov-type numerical formulation lies essentially on Finite Volume (FV) piecewise-constant information that is evolved, in time, by means of (spatial) inter-cell spatial fluxes combining nonlinear wave propagations [5]. In this sense, the formulation is local and first-order accurate; or may be said to allow the evolution of single-scale of local accuracy. Shallow water models based on a local first-order FV formulation are widespread [6,7]. Nowadays, they are being improved for practical modelling applications supported by their simplicity, conceptual soundness and locality [8–11]. Second- and higher-order FV methods have also been designed with a more academic focus [10–16].

* Corresponding author at: Civil & Structural Engineering, University of Sheffield, Sheffield, UK.
E-mail addresses: g.kesserwani@shef.ac.uk (G. Kesserwani), d.caviedes@sheffield.ac.uk (D. Caviedes-Voullième), gerhard@igpm.rwth-aachen.de (N. Gerhard), mueller@igpm.rwth-aachen.de (S. Müller).

http://dx.doi.org/10.1016/j.cma.2015.05.016

However, such designs have often rested on extrinsic non-local reconstruction of polynomial estimates from the local piecewise-constant evolution data yielding wider calculation stencils, which complicates coping with many other issues including parallelization, boundary conditions, mesh adaptation and wetting and drying [17,18]. Consequently, local first-order FV shallow water models seem to be more useable to support realistic applications despite requiring fine mesh resolution to alleviate their inevitable diffusivity [19,20].

In recent years, the Discontinuous Galerkin (DG) method has emerged as a more thorough alternative for locally solving conservation laws of the shallow water equations with higher accuracy [21–27]. The DG method further involves finite element weak formulation to – inherently from conservation principles – shape a piecewise-polynomial solution over each local discrete cell, via local basis functions. On this basis, the DG polynomial accuracy is spanned by a set of coefficients, describing accuracy information, which are *all* locally evolved in time from conservation principles at the discrete level, with an arbitrary order of accuracy. A DG-based shallow water model appeals in providing higher quality solutions on very coarse meshes than a traditional finite volume counterpart, but is comparatively expensive to run and imposes a more restrictive stability condition for the CFL number [28,29].

To reduce the costs of the DG method, given its locality convenience, it is often adapted on meshes encompassing various scales of spatial resolution, where the mesh is refined around highly dynamic flows and coarsened elsewhere [22,30]. Nonetheless, a conventional "*decoupled mesh vs. solution adaptation*" strategy is not without compromises as such [22,31,32]. For example; firstly, studies including the one by Nemec & Aftosmis [33] clearly evidence that the coarse solution must be fine enough to allow the adaptive solution to sense triggering events. Secondly, typical adaptation strategies relies on extrinsic criteria (e.g. gradient sensors) with mixed (coarsening and refinement) parameters, which are sensitive to each other and user-selected, thus leading to either excessive or inappropriate resolution; moreover, practically speaking, further mesh manipulation efforts are needed to refine the mesh around a wet/dry front [30]. Lastly, the DG formulation, although it allows local scaling of accuracy information, only operates on a single-scale of mesh resolution; thus it cannot, by design, allow transfer of information across compound resolution scales in conventional mesh adaptation strategies and direct (quantitative) control over the adaptive solution error quality [31].

This paper explores the design and application of a new and even more sophisticated Godunov-type shallow water numerical model formulation, which: (a) conceptually embeds locality, accuracy and resolution and, (b) allows self-adaptability of local resolution scales driven by one user-parameter-input. The new underlying formulation merges MultiWavelets (MW) with the DG method, referred hereafter to MWDG. MW extend conventional wavelets to enable compression of information to a *set of functions* on a *local* interval [34]; they offer a sound mechanism for transforming single-scale *local basis functions* into multi-scale bases and are entirely consistent with the discontinuous solution structure of the DG method. By this means, the local DG polynomial solution can be described as a *coarse scale information* encapsulating high-order fluctuations, or multiwavelet coefficients, which allow reaching *higher-resolution information* when non-zeroed within the local solution description. In addition, the magnitude of multiwavelets allows resolution adaptivity to be achieved by cancelling/adding detail-coefficients that fall below a certain threshold. Some preliminary forms of an MWDG merge have been reported before [35,36] with no clear focus on (i) how adaptivity is achieved in this novel context and (ii) what would be the potential merit pertaining to shallow flow modelling. More recently, an MWDG form for general homogeneous hyperbolic conservation laws addressing carefully issue (i) has been derived in [37,38]. This paper proposes an alternative MWDG formulation for the case of the 1D *non-homogeneous* shallow water equations with topography source terms, and with more specific technical focus on issues of relevance to *conservative* modelling of shallow water flows with discontinuities and/or over steep terrain. New qualitative and quantitative results addressing issue (ii) are presented and discussed offering novel insights into the potential merit of the MWDG to the field of Computational Hydraulics.

2. Shallow water equations (SWE)

The one-dimensional (1D) SWE can be expressed in the following conservative vector form:

$$\partial_t \mathbf{U} + \partial_x \mathbf{F}(\mathbf{U}) = \mathbf{G}(\mathbf{U}) \tag{1}$$

With $\mathbf{U} = [h \quad hu]^{\mathrm{T}}$, $\mathbf{F}(\mathbf{U}) = \left[hu \quad u^2h + gh^2/2\right]^{\mathrm{T}}$ and $\mathbf{G}(\mathbf{U}) = [0 \quad -gh\partial_x z]^{\mathrm{T}}$ are vectors of the unknowns (or conserved quantities), the flux and the topography source term, where (x, t) are the space–time coordinates, $h(x, t)$ is

the water depth (in m), hu (in m^2/s) is the unit width discharge, $u(x,t)$ being the depth-averaged velocity (in m/s), g (in m/s^2) the acceleration due to gravity and $z(x)$ is the topography function.

3. Single-resolution 1D discontinuous Galerkin (DG) formulation

A 1D domain $[x_{\min}, x_{\max}]$ is subdivided into N uniform and non-overlapping cells $\{I_i\}_{i=1,\dots,N}$ with $I_i = [x_{i-1/2}, x_{i+1/2}]$, of size $\Delta x = x_{i+1/2} - x_{i-1/2}$ and centre $x_i = (x_{i+1/2} + x_{i-1/2})/2$. A local approximation, $\mathbf{U_h}$, is sought in the space of polynomials of degree at most p (i.e. denoted by V_p) defined on each cell I_i by a local basis of polynomial functions $\mathbf{\Phi}^i = \{\varphi_{i,0}, \varphi_{i,1}, \dots, \varphi_{i,p}\}$, which is selected to be orthonormal (to decouple the system into a set of detached ODEs). Thus, on I_i, the local solution can be expanded as:

$$\mathbf{U_h}(x,t)|_{I_i} = \sum_{l=0}^{p} \mathbf{S}_{i,l}(t)\varphi_{i,l}(x) \quad (x \in I_i) \tag{2}$$

where $\{\mathbf{S}_{i,l}(t)\}_{l=0,\dots,p}$ are $(p+1)$ coefficients defining a $(p+1)$-order polynomial solution over cell I_i. These coefficients are initialized by projecting a given initial condition $\mathbf{U}_0(x) = \mathbf{U}(x,0)$ onto the basis $\mathbf{\Phi}^i$, i.e. $\mathbf{S}_{i,l}(0) = \langle \varphi_{i,l}, \mathbf{U}_0 \rangle$ [39].

To evolve in time each of these coefficients, the finite element weak formulation is applied. Namely, multiplying (1) by the local basis functions, integrating over the domain, and removing the flux derivative term via integration by parts, the system becomes:

$$\begin{aligned} &\int_{I_i} \partial_t \mathbf{U}(x,t)\varphi_{i,l}(x)dx - \int_{I_i} \mathbf{F}\left(\mathbf{U}(x,t)\right) \partial_x \varphi_{i,l}(x)dx \\ &\quad + \left[\mathbf{F}\left(\mathbf{U}(x^-_{i+1/2},t)\right)\varphi_{i,l}(x^-_{i+1/2}) - \mathbf{F}\left(\mathbf{U}(x^+_{i-1/2},t)\right)\varphi_{i,l}(x^+_{i-1/2})\right] \\ &= \int_{I_i} \mathbf{G}\left(\mathbf{U}(x,t)\right)\varphi_{i,l}(x)dx \end{aligned} \tag{3}$$

Incorporating further the local polynomial expansion (2) into Eq. (3), and a numerical flux function $\tilde{\mathbf{F}}$ for solving the Riemann problem defined by inter-cell solution discontinues, the local semi-discrete DG formulation becomes:

$$\begin{aligned} \frac{d}{dt}\mathbf{S}_{i,l}(t) = -\Big[&\tilde{\mathbf{F}}\left(\mathbf{U_h}(x^-_{i+1/2},t), \mathbf{U_h}(x^+_{i+1/2},t)\right)\varphi_{i,l}(x^-_{i+1/2}) - \tilde{\mathbf{F}}\left(\mathbf{U_h}(x^-_{i-1/2},t), \mathbf{U_h}(x^+_{i-1/2},t)\right)\varphi_{i,l}(x^+_{i-1/2}) \\ &- \int_{I_i} \mathbf{F}\left(\mathbf{U_h}(x,t)\right)\partial_x\varphi_{i,l}(x)dx - \int_{I_i} \mathbf{G}\left(\mathbf{U_h}(x,t)\right)\varphi_{i,l}(x)dx\Big] \end{aligned} \tag{4}$$

Here, we particularly select the desired $\mathbf{\Phi}^i$ by exploiting the Legendre basis of polynomials, denoted by $\mathbf{P}_p = \{P_l\}_{l=0,1,\dots,p}$, which is here orthonormal on $L_2([-1,1])$ (i.e. to obtain an identity mass matrix) as follows:

$$\varphi_{i,l}(x) = \sqrt{\frac{2}{\Delta x}}\varphi_l\left(\frac{x - x_i}{\Delta x/2}\right) \quad (x \in I_i), \quad \text{with } \varphi_l(\xi) = \sqrt{\frac{2l+1}{2}}P_l(\xi) \quad (\xi \in [-1,1]) \tag{5}$$

For this particular configuration, the local semi-discrete DG formulation for updating each lth coefficient ($l = 0, 1, \dots, p$) of polynomial accuracy over a cell I_i reads:

$$\begin{aligned} \frac{d}{dt}\mathbf{S}_{i,l}(t) = -\sqrt{\frac{2}{\Delta x}}\sqrt{\frac{2l+1}{2}}\Bigg\{&\left[\tilde{\mathbf{F}}_{i+1/2} - (-1)^l\tilde{\mathbf{F}}_{i-1/2}\right] \\ &- \int_{-1}^{+1} \mathbf{F}\left(\mathbf{U_h}\left(x_i + \frac{\Delta x}{2}\xi, t\right)\right)\frac{dP_l}{d\xi}(\xi)d\xi - \int_{-1}^{+1} \mathbf{G}\left(\mathbf{U_h}\left(x_i + \frac{\Delta x}{2}\xi, t\right)\right)P_l(\xi)d\xi\Bigg\} \end{aligned} \tag{6}$$

In (6), $\tilde{\mathbf{F}}_{i+1/2} = \tilde{\mathbf{F}}\left(\mathbf{U_h}(x^-_{i+1/2},t), \mathbf{U_h}(x^+_{i+1/2},t)\right)$ denotes the Riemann flux evaluation at interface $x_{i+1/2}$ separating cells I_i and I_{i+1}. The local integral term is computed by the Gauss–Legendre rule with $(p+1)$ quadrature points.

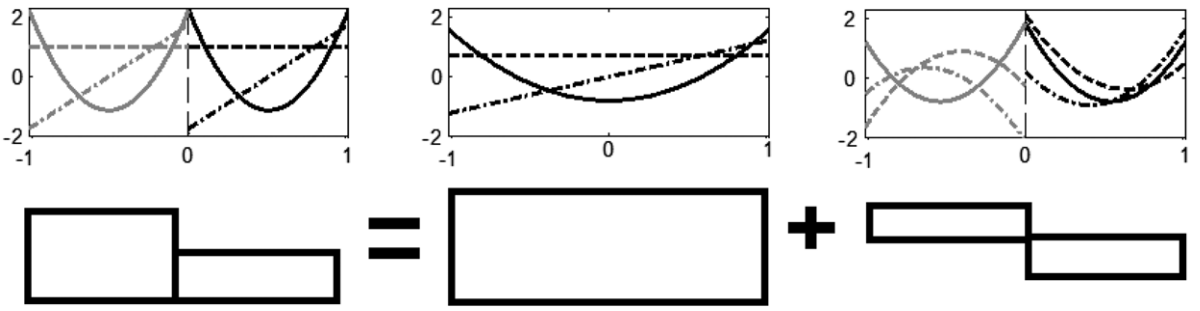

Fig. 1. Local (scaled) Legendre bases of functions ($p = 2$) at resolution level 1 decomposed as sum of scaling functions of the (mother) basis at resolution level 0 and the multiwavelet bases of details.

Finally, time integration is achieved by locally applying a $(p + 1)$-stages explicit Runge–Kutta time mechanism to solve the ODEs in (6)—with a CFL number less than $1/(2p + 1)$ for stability [39].

4. Multiwavelet decomposition of functions on the reference interval

In order to introduce a multi-resolution analysis on the reference interval $[-1, 1]$, a hierarchy of nested grids, $\{I_j^n\}_{j=0,1,\ldots,2^n-1}$ $(n \geq 0)$, is first defined by dyadic sub-division of the reference interval, i.e. $I_j^n = [-1 + 2^{-n+1}j, -1 + 2^{-n+1}(j + 1)]$. V_p^n denotes the space of piecewise polynomial functions of degree at most p defined on an arbitrary sub-interval I_j^n at resolution n. The spaces V_p^n $(n \geq 0)$ have dimension 2^n $(p + 1)$ and possess the nested property $V_p^0 \subset V_p^1 \subset \cdots \subset V_p^n \subset \cdots$. Within this hierarchy, the local basis functions at resolution n (defined in space V_p^n) are the coarse details of the local basis functions at resolution $n + 1$ (defined in V_p^{n+1}). This means that the support of the local basis functions in V_p^{n+1} is half the size of the support of local basis functions in V_p^n such that double resolution is possible (see Fig. 1). Given an orthonormal basis $\mathbf{\Phi} = \{\varphi_0, \varphi_1, \ldots, \varphi_p\}$ of $(p + 1)$ functions spanning the space V_p^0 on $[-1; +1]$, a sub-space V_p^n supported on I_j^n is spanned by the basis $\mathbf{\Phi}_j^n = \{\varphi_{j,0}^{(n)}, \varphi_{j,1}^{(n)}, \ldots, \varphi_{j,p}^{(n)}\}$ containing 2^n $(p + 1)$ functions, which are obtained from the mother basis functions $\mathbf{\Phi}$ by translation and dilatation:

$$\mathbf{\Phi}_j^n(x) = 2^{n/2}\mathbf{\Phi}\left(2^n(x + 1) - 2j - 1\right) \quad (j = 0, \ldots, 2^n - 1 \text{ and } x \in I_j^n) \tag{7}$$

In Eq. (7), j represents the translation, or shifting factor, across sub-intervals $\{I_j^n\}_{j=0,1,\ldots,2^n-1}$ and 2^n is the dilatation factor [40].

The ***multiwavelets*** sub-space W_p^n $(n \geq 0)$ comes into play as the orthogonal complement of V_p^n in V_p^{n+1}, i.e. $V_p^n \oplus W_p^n = V_p^{n+1}$ and $V_p^n \perp W_p^n$ (see Fig. 1). From a mother basis of multiwavelets $\mathbf{\Psi} = \{\psi_0, \psi_1, \ldots, \psi_p\}$, defined on $[-1, 1]$, spanning W_p^0, local multiwavelet bases spanning W_p^n, i.e. $\mathbf{\Psi}_j^n = \{\psi_{j,0}^{(n)}, \psi_{j,1}^{(n)}, \ldots, \psi_{j,p}^{(n)}\}$, can also be obtained by translation and dilation:

$$\mathbf{\Psi}_j^n(x) = 2^{n/2}\mathbf{\Psi}\left(2^n(x + 1) - 2j - 1\right) \quad (j = 0, \ldots, 2^n - 1 \text{ and } x \in I_j^n) \tag{8}$$

Multiwavelets form a set of functions which, together with a set of scaling functions, can be used to reconstruct or decompose an arbitrary function $f(x)$ – assumed scalar since the process can be applied for the vector case in a component-wise manner – across multiple scales of resolution. This is because V_p^n can be split into $(n+1)$ orthogonal subspaces as:

$$V_p^n = V_p^0 \oplus W_p^0 \oplus W_p^1 \oplus \cdots \oplus W_p^{n-1} \tag{9}$$

Considering the twofold facet of (9), $f(x)$ can be described *either* by a single-scale projection onto space V_p^n, i.e.:

$$P_p^n[f](x) = \sum_{j=0}^{2^n-1}\sum_{l=0}^{p} s_{j,l}^{(n)}\varphi_{j,l}^{(n)}(x) \tag{10}$$

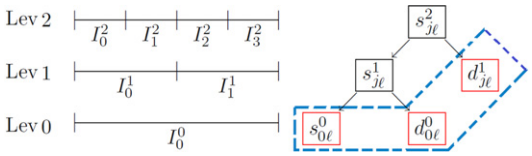

Fig. 2. Up to two levels of resolution over $[-1, 1]$ at which the single-scale coefficients at level 1, for example, can be obtained by the single-scale coefficients of level 0 and the multiwavelet coefficients.

or by involving multiwavelet detail-coefficients, obtained by (11):

$$Q_p^n[f](x) = P_p^{n+1}[f](x) - P_p^n[f](x) = \sum_{j=0}^{2^n-1} \sum_{l=0}^{p} d_{j,l}^{(n)} \psi_{j,l}^{(n)}(x) \tag{11}$$

By recursive use of Eq. (11), the equivalent projection of $f(x)$ onto $V_p^0 \oplus W_p^0 \oplus W_p^1 \oplus \cdots \oplus W_p^{n-1}$ can be obtained, i.e.:

$$P_p^{n+1}[f](x) = \sum_{l=0}^{p} s_{0,l}^{(0)} \varphi_l(x) + \sum_{m=0}^{n} \sum_{j=0}^{2^m-1} \sum_{l=0}^{p} d_{j,l}^{(m)} \psi_{j,l}^{(m)}(x) \tag{12}$$

The representation, in (12), is called *multi-scale decomposition* in which coefficients $\{s_{0,l}^{(0)}\}$ can be viewed as coarse information at resolution ($n = 0$), i.e. the context signal, on top of which its higher-order fluctuations $\{d_{j,l}^{(m)}\}$ live, or details, which allow to escalade to higher resolutions ($n > 0$) once non-zeroed within Eq. (12); thus allows to access or recuperate the higher resolution coefficients $\{s_{j,l}^{(n)}\}$ (see Fig. 2).

4.1. Two-scale transformation for down- and up-scaling local information

From the properties of the scaling and multiwavelet functions, a two-scale transformation can be derived to promote, or demote, the local solution expansion between two successive resolution levels. To simplify presentation, we present the two-scale transformation between level 0 and level 1. Two different types of coefficients are needed: low-pass filter coefficients and high-pass filter coefficients (derived from the local scaling functions). These coefficients are from the nested relationship between subspaces. Namely, for all the scaling functions $\varphi_k \in V_p^0$, $k = 0, 1, \ldots, p$, there exist coefficients $\{h_{k,l}^{(0)}\}_{l=0,1,\ldots,p}$ and $\{h_{k,l}^{(1)}\}_{l=0,1,\ldots,p}$ such that [40]:

$$\varphi_k(x) = \sqrt{2} \sum_{l=0}^{p} \left(h_{k,l}^{(0)} \varphi_l(2x) + h_{k,l}^{(1)} \varphi_l(2x-1) \right) \tag{13}$$

Similarly, for all multiwavelets $\psi_k \in W_p^0$, there exist coefficients $\{g_{k,l}^{(0)}\}_{l=0,1,\ldots,p}$ and $\{g_{k,l}^{(1)}\}_{l=0,1,\ldots,p}$ such that:

$$\psi_k(x) = \sqrt{2} \sum_{l=0}^{p} \left(g_{k,l}^{(0)} \varphi_l(2x) + g_{k,l}^{(1)} \varphi_l(2x-1) \right) \tag{14}$$

The coefficients from (13) are typically assembled in matrices $\mathbf{H_0} = \{h_{k,l}^{(0)}\}_{k,j}$ and $\mathbf{H_1} = \{h_{k,l}^{(1)}\}_{k,j}$ which are the low-pass filters; whereas coefficients from (14) are contained in matrices $\mathbf{G_0} = \{g_{k,l}^{(0)}\}_{k,j}$ and $\mathbf{G_1} = \{g_{k,l}^{(1)}\}_{k,j}$, which are the high-pass filters. These coefficients can be calculated through Gauss–Legendre quadrature to take the following forms:

$$h_{k,l}^{(0)} = \frac{1}{\sqrt{2}} \sum_{G=0}^{p} w_G \varphi_k \left(\frac{\xi_G}{2} \right) \varphi_l(\xi_G) \tag{15a}$$

$$h_{k,l}^{(1)} = \frac{1}{\sqrt{2}} \sum_{G=0}^{p} w_G \varphi_k \left(\frac{\xi_G + 1}{2} \right) \varphi_l(\xi_G) \tag{15b}$$

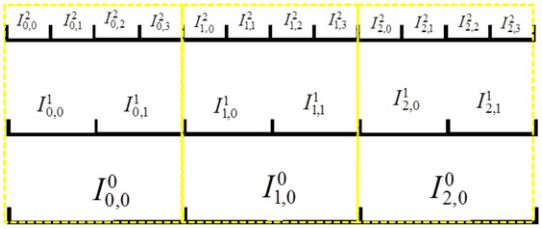

Fig. 3. Example of a multi-resolution grid hierarchy $(I^n_{i,j})_{i,j}$ over three mother cells and up to level 2 of resolution, at which the multi-scale DG formulation is derived.

$$g^{(0)}_{k,l} = \frac{1}{\sqrt{2}} \sum_{G=0}^{p} w_G \psi_k \left(\frac{\xi_G}{2} \right) \psi_l (\xi_G) \tag{15c}$$

$$g^{(1)}_{k,l} = \frac{1}{\sqrt{2}} \sum_{G=0}^{p} w_G \psi_k \left(\frac{\xi_G + 1}{2} \right) \psi_l (\xi_G) \tag{15d}$$

where w_G and ξ_G are respectively the same Gauss–Legendre weights and nodes used for integral approximations.

To demote information, the low-pass filters is first used to combine two sets of coefficients, relevant to each shift at resolution level 1, to form a new set of coefficient relative to resolution 0:

$$\left[\{s^{(0)}_{j,l}\}_l \right]_{j=0} = \mathbf{H_0} \left[\{s^{(1)}_{j,l}\}_l \right]_{j=0} + \mathbf{H_1} \left[\{s^{(1)}_{j,l}\}_l \right]_{j=1} \tag{16a}$$

Then, by applying the high-pass filter to the same coefficients at level 1, their details at resolution 0 are produced and stored (for possible use):

$$\left[\{d^{(0)}_{j,l}\}_l \right]_{j=0} = \mathbf{G_0} \left[\{s^{(1)}_{j,l}\}_l \right]_{j=0} + \mathbf{G_1} \left[\{s^{(1)}_{j,l}\}_l \right]_{j=1} \tag{16b}$$

Since the transform is invertible, it is also used for promoting coefficients, from a single resolution at level 0 into two shifts in resolution at level 1. Namely, this is done by means of the compound transform formula involving the inverse of both filters:

$$\left[\{s^{(1)}_{j,l}\}_l \right]_{j=0} = \mathbf{H_0^{-1}} \left[\{s^{(0)}_{j,l}\}_l \right]_{j=0} + \mathbf{G_0^{-1}} \left[\{d^{(0)}_{j,l}\}_l \right]_{j=0} \tag{17a}$$

$$\left[\{s^{(1)}_{j,l}\}_l \right]_{j=1} = \mathbf{H_1^{-1}} \left[\{s^{(0)}_{j,l}\}_l \right]_{j=0} + \mathbf{G_1^{-1}} \left[\{d^{(0)}_{j,l}\}_l \right]_{j=0} \tag{17b}$$

By recursive application of Eq. (16), resp. Eq. (17), the expansion coefficients describing a local signal can be comprehensively lifted from highest to lowest resolution, or vice versa.

5. Multiwavelets with the discontinuous Galerkin method (MWDG)

This section describes how the DG scheme (Section 3) and the MW decomposition (Section 4) are combined. For this purpose, the multi-resolution analysis is applied to each cell I_i of the baseline discretization producing a fully-scalable DG formulation. By means of the multiwavelet coefficients, a heterogeneous grid involving a selection of resolution levels is determined on which the time evolution is actually performed.

5.1. Local multi-scale DG formulation

Now each cell $I_i = [x_{i-1/2}, x_{i+1/2}]$ is orderly subdivided into 2^n sub-intervals $(I^n_{i,j})_{j=0,1,\ldots,2^n-1}$ such that: $I^n_{i,j} = [x_{i-1/2} + \Delta x^{(n)} j,\ x_{i-1/2} + \Delta x^{(n)}(j+1)]$ with the local spatial-resolution $\Delta x^{(n)} = 2^{-n}\Delta x$, and a sub-cell centre denoted by $x^{(n)}_{i,j} = x_{i-1/2} + \Delta x^{(n)}(j + 1/2)$ (see Fig. 3). Note that the sub-index i is introduced to further refer to the mother cell of interest. Here, a local approximation, $\mathbf{U_h}$, is sought in the space of polynomials of degree at most p but at an arbitrary level n (i.e. $\mathbf{U_h} \in V^n_p$), which is also spanned by an *orthonormal* and *compactly-supported*

basis of polynomial functions $\mathbf{\Phi}^n_{i,j} = \{\varphi^{(n)}_{i,j,0}, \varphi^{(n)}_{i,j,1}, \ldots, \varphi^{(n)}_{i,j,p}\}$ defined on each sub-cell $I^n_{i,j}$. On this basis, the local solution $\mathbf{U_h}$ reads:

$$\mathbf{U_h}(x,t)|_{I^n_{i,j}\subset I_i} = \sum_{l=0}^{p} \mathbf{S}^{(n)}_{i,j,l}(t)\ \varphi^{(n)}_{i,j,l}(x) \quad \left(x \in I^n_{i,j}\right) \tag{18}$$

with the initial coefficients $\mathbf{S}^{(n)}_{i,j,l}(0) = \langle \mathbf{U}_0, \varphi^{(n)}_{i,j,l}\rangle$. Reworking (4), via taking the basis of functions $\mathbf{\Phi}^n_{i,j}$ so that it is orthonormal on $L_2(I^n_{i,j})$, i.e. we take $\{\varphi^{(n)}_{i,j,l}\}_l$ from the scaled Legendre basis:

$$\varphi_{i,j,l}(x) = \sqrt{\frac{2}{\Delta x^{(n)}}}\varphi_l\left(\frac{x - x^{(n)}_{i,j}}{\Delta x^{(n)}/2}\right) \tag{19}$$

The following *scale-dependent* semi-discrete local DG operators are obtained:

$$\frac{d}{dt}\mathbf{S}^{(n)}_{i,j,l} = -\sqrt{\frac{2}{\Delta x^{(n)}}}\sqrt{\frac{2l+1}{2}}\left\{\tilde{\mathbf{F}}^{i,(n)}_{j+1/2} - (-1)^l\tilde{\mathbf{F}}^{i,(n)}_{j-1/2} - \int_{-1}^{-1}\mathbf{F}\left(\mathbf{U_h}\left(x^{(n)}_{i,j} + \frac{\Delta x^{(n)}}{2}\xi\right), t\right)\frac{dP_l}{d\xi}(\xi)\,d\xi\right.$$
$$\left. - \int_{-1}^{-1}\mathbf{G}\left(\mathbf{U_h}\left(x^{(n)}_{i,j} + \frac{\Delta x^{(n)}}{2}\xi\right), t\right)P_l(\xi)\,d\xi\right\} \tag{20}$$

In (20), $\tilde{\mathbf{F}}^{i,(n)}_{j+1/2}$ is the Riemann flux evaluation across the inner interface between sub-cells $I^n_{i,j}$ and $I^n_{i,j+1}$. The integral term evaluation and all others operations relevant to the standard DG method are here dealt with in a similar way.

5.2. Adaptive selection of active resolution scales

In the intended MWDG context, the notion of grid adaptivity refers to how to selectively choose those resolution levels of the compressed grid hierarchy at which Eq. (20) should be applied. This selection process is performed by acting on the multiwavelet coefficients; therefore a set of the significant details is introduced – among the multiwavelet coefficients – and will be denoted by: $\mathrm{H} \in \{(i,s,m), 0 \le i \le N, 0 \le s \le 2^m - 1\}$. From this set, it is possible to determine those sub-cells across the different resolution that need to be active within the adaptive grid, i.e. $\{I^m_{i,s}\}_{(i,s,m)\in\mathrm{H}}$ such that $\bigcup_{(i,s,m)\in\mathrm{H}}\{I^m_{i,s}\} = [x_{\min}, x_{\max}]$.

In the proposed adaptive context, the local polynomial approximation of the flow vector, i.e. $\mathbf{U_h}$, over a cell $I_{i,s}$ is expressed as in Eq. (12) by a multi-scale decomposition up to a highest resolution n, but with an extra index 'i' referring to the mother cell and vector coefficients $\mathbf{S}^{(0)}_{i,0,l}$ and $\mathbf{D}^{(m)}_{i,s,l}$. Under this shape, detail coefficients at a resolution $m \le n$, $\mathbf{D}^{(m)}_{i,s,l}$ become increasingly smaller with increasing level of spatial resolutions. Thus, solution-driven adaptivity can be achieved by *only* measuring the magnitude of multiwavelet (or detail) coefficients according to a prescribed threshold-value ε. Although there is no unique choice for ε, a strategy for choosing it such that to preserve the same quality as a *reference fine uniform mesh* is feasible [37]. This *reference mesh* is actually formed by a single-scale expansion, i.e. as in Eq. (11), at resolution level n (i.e. finest resolution accessible); it is only needed to carry out the multi-resolution analysis and no actual computations need to be performed on it. Following [38], the h-adaptive MWDG approach used here mainly consists of three key steps: *Prediction* (for refinement), *Multi-scale DG update* on the predicted mesh and *Hard thresholding* (for coarsening of both predicted mesh and updated solution).

5.2.1. Prediction (refinement)

After each time evolution step, *prediction* is introduced to identify those regions where high resolution will be needed to guarantee that no significant (future) features of the solution are lost. *Prediction* can only be based on the information available at the present time level. If at least one component of $\mathbf{D}^{(m)}_{i,s,l}$ (i.e. relevant to any conservative variable or accuracy level $l = 0, 1, \ldots, p$) is detected significant, then the vector will be retained. The detection process is performed by first standardizing all detail coefficients so that their magnitude does not exceed unity, and then comparing them relating to the threshold-value. These measures for *prediction* can be achieved via the criteria

described below:

$$\max_{(i,s,m)\in \mathrm{H}} \left(\frac{\left|\mathbf{D}_{i,s,l}^{(m)}\right|}{\max\left\{ \max_{(i,s,m)\in \mathrm{H}} \left(\left|\mathbf{S}_{i,s,0}^{(m)}\right| \right), \sqrt{\Delta x^{(m)}} \right\}} \right) > \varepsilon_m = 2^{m-L}\varepsilon \tag{21}$$

where L is the maximum number of refinement levels. After (21) identifies those cells with significant details, their neighbouring cells on the same level are also set significant, i.e. they will be refined. It is found also important to retain the corresponding details at the higher level $(m+1)$ since gradients may steepen due the formation of shocks, which is done by the criterion below:

$$\max_{(i,s,m)\in \mathrm{H}} \left(\frac{\left|\mathbf{D}_{i,s,l}^{(m)}\right|}{\max\left\{ \max_{(i,s,m)\in \mathrm{H}} \left(\left|\mathbf{S}_{i,s,0}^{(m)}\right| \right), \sqrt{\Delta x^{(m)}} \right\}} \right) > 2^{\bar{M}+1}\varepsilon_m \tag{22}$$

In (22), $\bar{M}$ represents the number of vanishing multiwavelet moments that is at least p due to orthogonality of the multiwavelets. This will ensure that polynomial accuracy is retained during the two-scale transformations.

Otherwise, $\mathbf{D}_{i,s,l}^{(m)}$ $(l = 0, 1, \ldots, p)$ is zeroed. This process is applied recursively and level-wise from coarsest to finest. Then, local polynomial solutions with nonzero detail coefficients are used, i.e. via application of (17a) and (17b), to up-scale grid data. At the end of this process, the appropriate multi-scale mesh, at which actual RKDG calculation needs to be performed, is identified, and is obtained by refining all outer cells containing significant details proceeding from coarsest to finest level.

5.2.2. *Multi-scale RKDG update*

The RKDG method, i.e. in Eq. (20), is applied to evolve the local polynomial coefficients on the predicted mesh. In this work, a RKDG3 formulation that evolves local quadratic-element solutions (i.e. $p = 2$) is applied in conjunction with a proper discretization of the topography source term, a conservative localization to the slope-limiter, and a suited Riemann solver. Each of these treatments has been carefully addressed in previous works, i.e. concerning the RKDG3 solutions to the SWEs on uniform grids, and has been directly transferred to this multi-scale version. These treatments are summarized below:

- Following the same idea as in [26], bed slope source term integration can properly be achieved by projecting the topography function onto the space local piecewise-linear polynomials (V_1^n) in a way that global continuity property is ensured. Furthermore, the topography projection is also compressed, analogous to how the flow variables are in Eq. (12), to allow the adaptivity to further consider the topography. That is, that the adaptivity will respond simultaneously to both the details of flow variables and terrain data.
- Equally, the notion of local and systematic slope limiting introduced in [26] is directly extended here. It relies on a localization step (to decide at which computational cells the *minmod* slope-limiter is to be applied) followed by a systematization step (to amend as minimum polynomial coefficients as needed), both of which generated from the polynomial solution itself. The strategy behind adopting this approach is to retain as high polynomial accuracy as possible, and thereby make the most of the conservation properties of the DG method [26].
- To more reliably communicate fluxes arising from the solution of local Riemann problems, the Roe [41] Riemann solver is identified to be one of the best choices for the RKDG solution to the non-homogeneous SWE [42], and is here adopted.

5.2.3. *Hard thresholding (coarsening)*

Following to the RKDG update, the *hard thresholding* step is found necessary to avoid excessive grid prediction that could have arisen during RKDG calculations. This step rests on strict zeroing to all those remaining vectors of detail coefficients that all their components fall below the (level-dependent) threshold-value; it has been achieved by

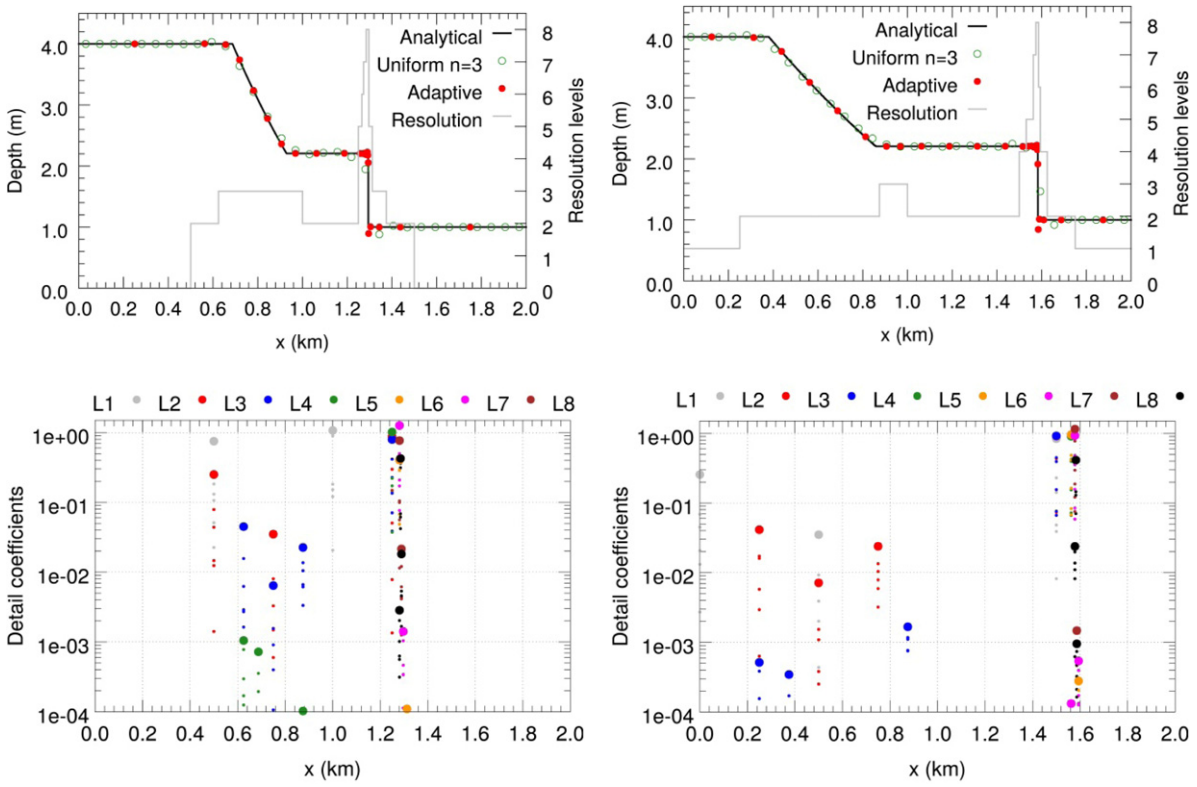

(a) Time = 50 s.

(b) Time = 100 s.

Fig. 4. Dam break test results for uniform mesh ($n = 3$) and adaptive mesh ($0 \leq n \leq 8$).

the condition below:

$$\tilde{\mathbf{D}}_{i,s,l}^{(m)} = \begin{cases} \mathbf{D}_{i,s,l}^{(m)} & \text{if } \max_{l} \left(\dfrac{\left|\mathbf{D}_{i,s,l}^{(m)}\right|}{\max\left\{ \max_{(i,s,m)\in H} \left(\left|\mathbf{S}_{i,s,0}^{(m)}\right| \right), \sqrt{\Delta x^{(m)}} \right\}} \right) > \varepsilon_m \\ 0 \end{cases} \tag{23}$$

After this step, down-scaling of the polynomial coefficients is carried out using the low-pass i.e. Eq. (16a), for grid information coarsening; whereas the high-pass filter, i.e. Eq. (16b), is applied to allow possible access (during the prediction step) to relevant underlying detail coefficients.

It is worth stressing that *hard thresholding* must be avoided at those cells where the grid has been initially refined around steep topographic features. This will provide a twofold gain: (1) retain the fine resolution at those zones of interest and (2) avoid re-establishment of the topography projection at each subsequent *prediction* step in order to avoid disturbing the well-balanced property.

6. Model validation

In this section, three 1D test cases are presented to illustrate the ability of the MWDG scheme to adaptively solve shallow water flow problems with reduced number of cells compared to the reference uniform mesh RKDG3 scheme. Two of the test cases are transient idealized dam-break cases over frictionless and horizontal beds; the third test considers steady transcritical flow over a hump with shock over non-flat topography. The results are compared against exact solutions, and RMSE (Root Mean Square Error) analysis is performed, where appropriate, to identify the extent to which the adaptive process retains the accuracy of the reference scheme.

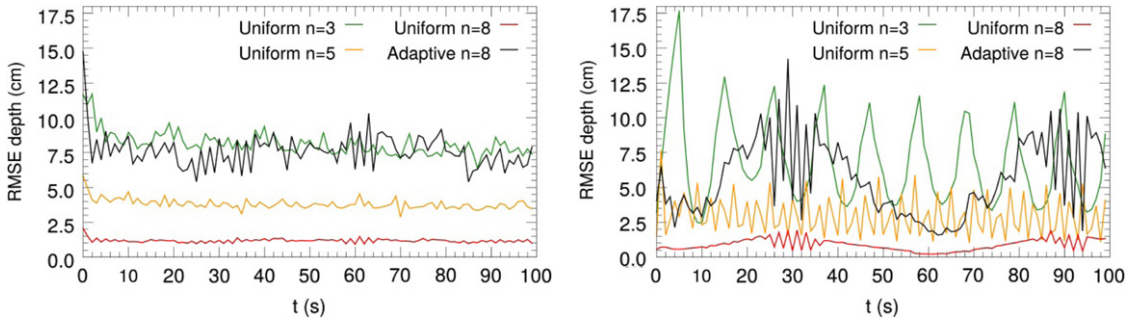

(a) Full polynomial solution.

(b) Mean value of the solution.

Fig. 5. Depth RMSE evolution for the dam break wet/wet test case.

The first test case is defined by a 2000 m long domain at which an imaginary dam separating two discontinuous still water levels, 4 m and 1 m, at 1000 m, is assumed to break, at $t = 0$ s. The dam-break wave produces (nonlinear) wave propagation patterns in both directions, namely, a shock wave propagating downstream and a rarefaction wave propagating upstream. The adaptive MDWG simulation is run using various resolutions, i.e. $0 \leq n \leq 8$. With such an MWDG setting, the coarsest resolution mesh ($n = 0$) contains only 4 cells whereas the highest resolution mesh comprises ($n = 8$) 1024 cells. For sake of comparisons, a number of mesh configurations with constant resolution of $n = 3$ (32 cells), $n = 5$ (128 cells) and $n = 8$ (1024 cells) are considered to run uniform mesh DG solutions. Figs. 4a and 4b show the results at $t = 50$ s and $t = 100$ s, respectively. Although the coarse mesh RKDG3 solution (i.e. at resolution $n = 3$) approximates the exact solution fairly well, more resolved predictions are seen for the adaptive MWDG solution at both times, even when both models entail similar local resolution level (e.g. Fig. 4a along with the rarefaction wave). Herein, most of the domain features required resolution level $n < 4$, except at the shock where the highest resolution level, 8, is attained. This peak of resolution is noted to track the transient movement of the shock (compare Figs. 4a *vs.* 4b); the relatively coarse resolution elsewhere – including through the rarefaction wave – is mainly associated with the choice of the ε-value (next paragraph). At those unperturbed regions, at the upstream and downstream end of the domain, resolution remained at very coarse levels ($n = 0$ at $t = 50$ s and at $n = 1$ at $t = 100$ s), which is expected given the very slow dynamics of the flow therein.

In addition, the lower row in Figs. 4a and 4b illustrates the relative behaviour of the detail coefficients, in terms of magnitude, i.e. the normalized details vector in Eqs. (21)–(23). At a cell and a certain level, the details vector contains six components (three for each conservative variable), which are represented in the figures by the dots. Of these dots, the *maximum* one is flagged with a bigger dot, which is actually the value used to trigger adaptivity. Note that the Y-axis scale does not reach zero, for clarity, since the majority of the detail coefficients are very small (non-significant). These figures are helpful to better understand how adaptivity is solely driven by the significance of the detail coefficients. For example, from Fig. 4a (lower row) it is clear that for $x < 0.4$, there are no significant detail coefficients at resolution level 1 or higher, therefore the mesh may remain at the coarsest resolution associated with level 0. However, at $x = 0.5$, the detail coefficients (in particular, their maximum values) are significant at both levels 1 and 2, which means that the mesh must be at least in level 2 of refinement at that position. At $x = 1.3$, there are significant details up to resolution level 8, which thus triggers up, locally, to level 8 of refinement.

To analyse the effects of adaptivity on accuracy, Fig. 5 displays the time history of the RMSE for the water depth predictions extracted from (i) the full polynomial solution information (Fig. 5a), and (ii) the mean values of the solution (Fig. 5b). Remarkably, the variation of the RMSE relevant to the full solution shows comparatively less sensitive evolution; whereas a more perturbed behaviour is observed for the RMSE predicted by acting only on the mean values of the local solution. In this sense, therefore the use of a local higher order RKDG scheme can be a benefit, namely when the local solution involves coarse resolution levels. In both cases, as expected, the adaptive RMSE evolution remained higher than the finest uniform mesh resolution available ($n = 8$) varying on average at the RMSE magnitude relevant to uniform resolution corresponding to $n = 3$. It is also expected that at some local areas the adaptive RMSE can be even higher due to the further coarsening in resolution ($n < 3$) allowed by the adaptive mesh setting.

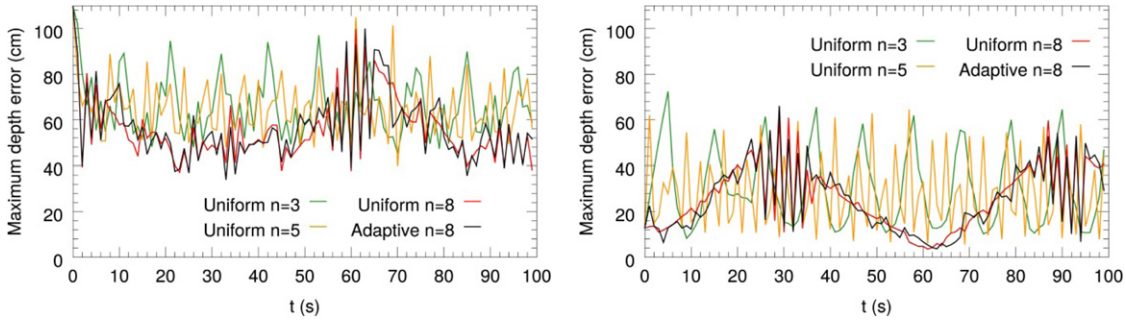

(a) Full polynomial solution.

(b) Mean value of the solution.

Fig. 6. Depth maximum error evolution for the dam break wet/wet test case.

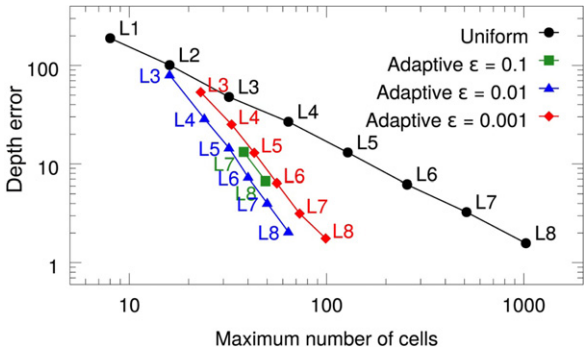

Fig. 7. Mesh convergence analysis of the adaptive MWDG approach exploring three choices for the threshold-value parameter (L = Number of levels).

To particularly demonstrate the error behaviour of the proposed MWDG adaptive strategy in handling sharp discontinuities, Fig. 6 shows the *maximum* local error evolution. Note that this error is bounded by the non-adaptive scheme and closely tracks the error of the solution with the highest resolution mesh $n = 8$. This is reasonable, since the adaptive strategy is deliberately designed to more accurately track shocks and allow lower resolution elsewhere, i.e. allows larger discretization errors compared to the highest resolution mesh results. Here, the variation of the maximum error calculated from the mean values of the solution is again seen to be more sensitive than those calculated based on the full polynomial solution.

Fig. 7 presents a mesh convergence analysis with systematic exploration to the threshold-values. The convergence study was computed for the RKDG3 method on eight uniform meshes (from $n = 1$ to $n = 8$, i.e., meshes containing 8 cells to 1024 cells) based on the L^1-error norm between the analytical and numerical depths. The same error metric was used to compute the MWDG adaptive solutions but with three different threshold-values: $\varepsilon = 0.1$, $\varepsilon = 0.01$ and $\varepsilon = 0.01$. In terms of relevance of the choice of the threshold-value, Fig. 7 brings about three notable points. First, the rate of convergence of the adaptive solutions is faster than for the uniform solutions. This in turn means that the adaptive schemes more efficiently achieve the same error magnitude produced on the fine uniform meshes (they require fewer cells). Second, an optimal choice for ε exists, that results in a similar error to that of the uniform mesh at the same level, and with the reduced number of cells. Herein, out of the three ε-values tested, 0.01 is found to be optimal in terms of allowing wider range of resolutions ($n \geq 3$) while keeping the error within the desired range (i.e. $\leq$uniform mesh error). Last, it is notable that, up to a certain order of magnitude, the choice of the ε-value becomes unimportant pertaining to preserve uniform mesh accuracy (e.g. here both $\varepsilon = 0.01$ and 0.001 allow acceptable range of accuracy at resolution levels $\geq$3) and the ideal choice is likely to be selected in favour of efficiency (i.e. here $\varepsilon = 0.01$). Thus, it can be said that the choice of the threshold-value is not particularly important, as long as it is in the correct order of magnitude. However, even though for the smaller $\varepsilon = 0.1$, which only allows acceptable error range for adaptive solutions with resolution levels $\geq$7, the MWDG predictions still offer an acceptable performance. This can be seen in the results of Figs. 4–6, which have been exclusively illustrated for the $\varepsilon = 0.1$. Of course,

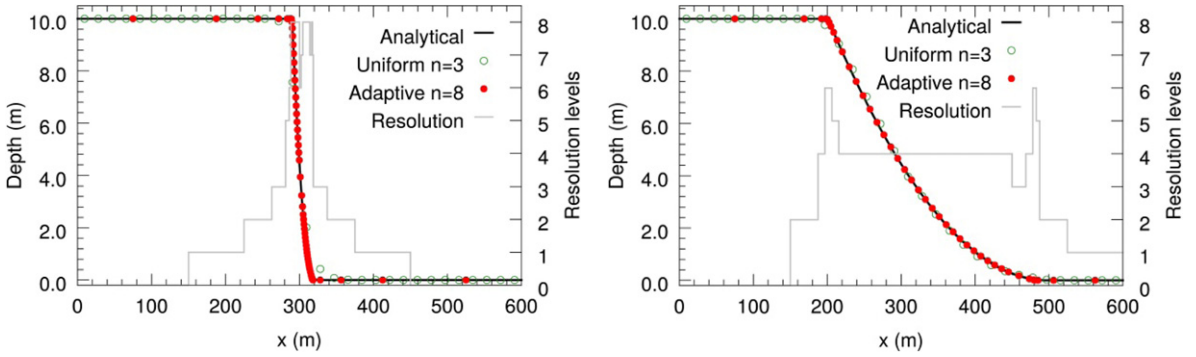

(a) Time = 1 s. (b) Time = 10 s.

Fig. 8. Dam break over dry bed results for uniform mesh ($n = 3$) and adaptive mesh ($n \leq 8$).

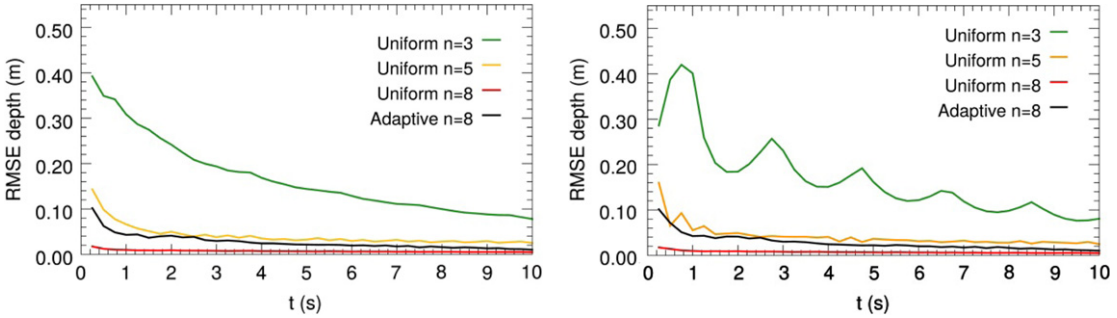

(a) Full polynomial solution. (b) Mean value of the solution.

Fig. 9. Depth RMSE evolution for the dam break wet/dry test case.

the choice of an ideal ε is further reliant on the order of accuracy of the RKDG scheme, the number of resolution levels allowed and relatedly the density of the baseline mesh; thus requires future exploration beyond the scope of this investigation. Furthermore, it must be noted that the number of levels must be chosen following the same criteria as in non-adaptive schemes, in order to achieve a sufficiently high accuracy for the features of interest in the solution. The adaptive scheme is then bounded by this choice, since it can only keep the accuracy of the reference, non-adaptive scheme on the highest level of resolution. These results indicate that the accuracy of the adaptive MWDG solution in predicting shock wave transients is comparable with the highest resolution available of the reference uniform mesh. In terms of computational cost, the number of cells involved in the adaptive computation (up to 100 s) varied between 35 and 48 cells with an overall average of 40 cells. This means that, at the very worst, the adaptive MWDG solution uses around 19 times less cells in the computation than the DG uniform mesh solution counterpart relevant to the highest resolution, i.e. reduces about 95% of the operational cost of the DG method.

The second test addresses the dam-break case involving a moving wet/dry front over a dry floodplain. The domain is 600 m long in which the dam separates a still water volume with a depth of 10 m (upstream) and a dry region. The same mesh settings are used as in the previous test and $\varepsilon = 0.1$. Fig. 8 shows the results at 1 s and 10 s for the adaptive $0 \leq n \leq 8$ along with the uniform mesh solutions at resolution $n = 3$, the local resolution levels and the exact solution. As Fig. 8 demonstrates, the adaptive MWDG solution is seen to trail very well the exact solution; at time 1s, the MWDG adaptive calculation reached the maximum level, 8, of refinement, in track with the supercritical dynamics of the wave front. At time 10 s, the MWDG model has more moderately adapted the resolution levels around the rarefaction tail and the wet/dry front; namely level 6 of resolution is selected to resolve these features whereas moderate resolution level, of 4, is noted to occur at the zone in-between them. Again, at the upstream and downstream ends, the MWDG adaptive model is observed to simulate those relatively unperturbed regions at the coarsest levels, 0 and 1, of resolution.

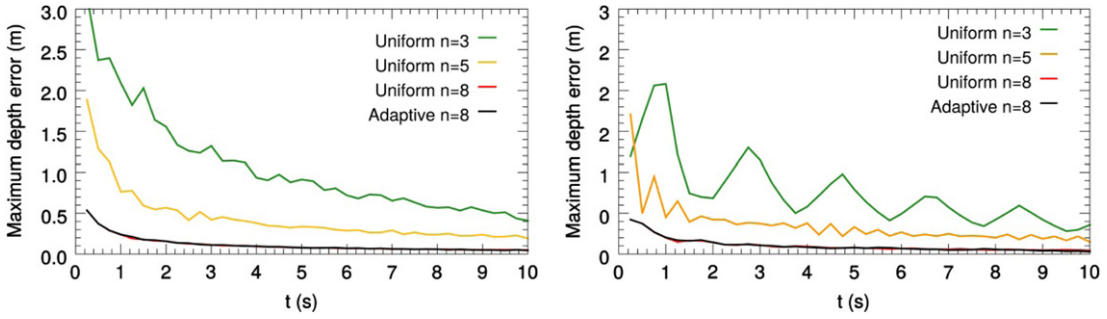

(a) Full polynomial solution. (b) Mean value of the solution.

Fig. 10. Depth maximum error evolution for the dam break wet/dry test case.

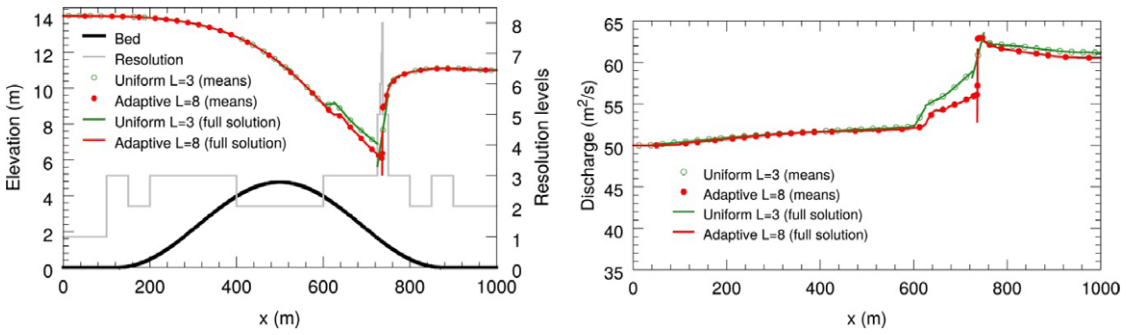

(a) Water surface elevation. (b) Discharge.

Fig. 11. Transcritical flow with shock at an intermediate time ($t = 25$ s) before convergence is reached.

Figs. 9 and 10 show the time history of the RMSE and the maximum error for the water depth variable produced by the adaptive simulation and the uniform mesh simulations. For this test case, the adaptive RMSE is seen to vary between those uniform mesh RMSE calculations at resolution levels $n = 5$ and $n = 8$. Here, the RMSE behaviour is observed to be rather identical despite of whether the full polynomial solution or the mean values are considered for the analysis, which is likely be associated with the shock-free nature of the numerical solution and reduced exposure to slope limiting. Most notably, the adaptive RMSE appears to closely converge to the RMSE predicted by the finest resolution available ($n = 8$) and, the maximum error of the adaptive solution matches almost exactly the one produced by the finest mesh (see Fig. 10). These findings thus signal that for shock-free, yet dynamic, shallow flow simulations, the adaptive MWDG prediction tends to asymptotically converge to the quality of the highest resolution available (i.e. comparing with the previous case). For this test, the average number of active cells is 72 and a maximum of 96 active cells recorded during the adaptive simulation and a minimum of 36 cells. This is, approximately 91% of decrease in cell number relative to the finest resolution uniform mesh simulation ($n \leq 8$, equivalent of 1024 cells).

A third test case is considered to show the ability of the adaptive scheme to achieve and converge towards a steady state flow including a transcritical flow transition, a shock occurrence and non-flat bump-like topography. The sinusoidal bump, defined over channel domain is 1000 m long, followed:

$$z(x) = 4.75 \sin^2\left(\frac{x - 1.25}{750}\pi\right) \tag{24}$$

At the coarsest level ($n = 0$), the mesh contains only five cells, and uniform DG solutions were computed with $n = 3$ (40 cells), $n = 5$ (160 cells) and $n = 8$ (1280 cells) to allow comparisons with the adaptive MWDG solution, which encompassed resolution levels with $0 \leq n \leq 8$ and $\varepsilon = 0.1$. Following [26], an upstream inflow is imposed by a unit discharge of 50 m^2/s whereas an outflow depth of 11 m is specified for the outflow boundary conditions. These imposed conditions were also used to initialize the simulations. An analytical solution of water depth can be obtained by solving the specific energy equation coupled locally with hydraulic jump equation. The numerical results,

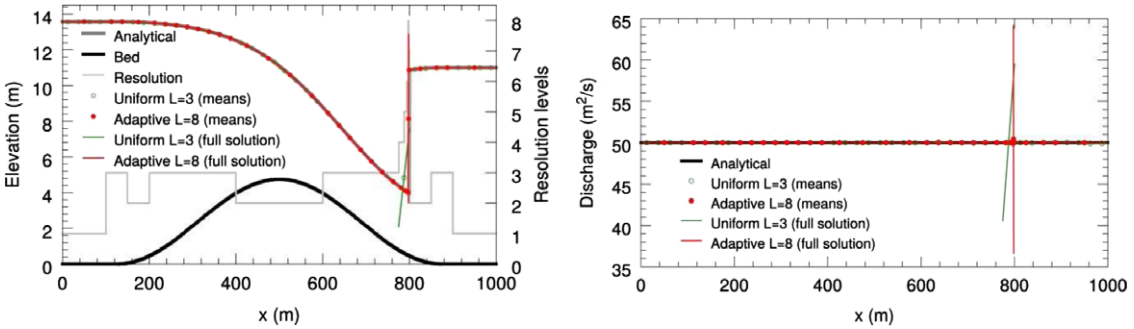

(a) Water surface elevation.

(b) Discharge.

Fig. 12. Transcritical flow with shock at after convergence ($t = 1000$ s).

considering both the full DG solutions and their averages, are shown in Figs. 11 and 12 at, respectively, an intermediate time state (at $t = 25$ s) and at time $t = 1000$ s, when the steady state has already been reached. For better clarity, only the uniform-mesh results for the case of $n = 3$ illustrated along with the adaptive MWDG solution including both full polynomial solution variation and the means.

Within both DG and MWDG models, as Fig. 11 discloses, it is seen that the local parabolic solutions are consistently varying towards the expected flow physics. Upstream of the critical flow zone and downstream of the shock, the local parabolic solutions are noted to vary smoothly and with no discontinuities visible to the naked eye, which is expected, given the smooth subcritical nature of the flow therein. At the supercritical zone and near the shock, the local parabolic solutions tend to be more linear and obviously reveal discontinuous behaviour (namely when approaching shock formation). These results confirm the ability of the adopted slope-limiting strategy to carefully treat the polynomial solution's coefficients even for the case of the MWDG adaptive scheme.

Fig. 12 shows the steady state computations achieved by the adaptive MWDG model and the selected uniform mesh variant jointly with the analytical depth and discharge profiles. Both models are observed to reproduce very well the analytical solution not only at the level of means but also considering the full solution evolution. However, the full local discharge solution to the shock remains linear in agreement with the shock presence in the solution of the depth variable. For the adaptive case, it is worth mentioning that the topography has also been treated by a similar spatial projection as the numerical MWDG solution in order to further allow mesh refinement to consider its presence while remaining driven by the same threshold-value (i.e. the vector $\mathbf{D}$ of details in Eqs. (21)–(23) further include three topographic detail coefficients). With this extra measure, the adaptive MWDG solution has clearly triggered a level 3 of refinement at its steepest gradient variations and level 2 in-between. At the boundaries, where the bed is flat and the flow is smooth, the mesh stabilized to level 1 of resolution. At the shock, the highest resolution 8 is selected showing a gradual downgrade of resolution to level 3 upstream of it and a direct drop to resolution 2 downstream of the shock. Gaps in resolution levels are also observed to occur at the boundaries, where the mesh goes from level 1 to 3 without having an intermediate level 2. It is important to comment that such gaps in downgrading resolution levels are allowed in the proposed MWDG adaptive strategy (i.e., exclude a regularization step such as with the case of the finite volume framework) and does not seem to cause problems given: (i) the availability of the full solution information over a local cell and (ii) self-driven solution adaptability that is entirely left to be decided by locally comparing the magnitude of the detail coefficients to the threshold-value.

Overall, results from the test cases show that the proposed adaptive MWDG framework excellently reproduces numerically conservative and accurate predictions to the shallow water equations with source terms. Importantly, the new model is shown to be able to self-decide appropriate resolution levels the dynamics of the flow, including the wet/dry front and the presence of non-flat topography, driven by a sole prescribed threshold-value parameter facilitating moderately both resolution coarsening and refinement.

7. Conclusions

This work has presented an adaptive Godunov-type numerical framework for solving the shallow water equations with topography source term. The new numerical formulation combines the multiwavelets with the discontinuous

Galerkin method to form the so-called MWDG merge. The appeal of the MWDG formulation is that it is locally-scalable for both accuracy and resolution scales. Another important feature of the MWDG framework is that it can be easily exploited to achieve dynamic grid resolution adaptivity from within the solution description and based on a single (threshold-value) parameter to sensibly achieve coarsening and refinement of resolution. The MWDG model has also been supported with features of relevance to conservative shallow flow modelling, i.e. a local and systematic slope limiting procedure, the Roe Riemann solver and piecewise polynomial well-balanced discretization to the topography source term, which have been found to be directly transferable from the standard RKDG method. Preliminary results (for a particular setting of the method with global third-order accuracy) reveal an excellent performance of the MWDG adaptive solution for two standard dam-break cases, under wet/wet and wet/dry conditions, and a steady transcritical flow with a shock over topography.

The 2D extension of the MWDG framework to solve general homogeneous conservation laws is direct for structured quadrilateral grids [43]. For the case of the shallow water with source terms, the work is ongoing to enable modelling of terrain data and wet/dry fronts in an entirely consistent way with the discontinuous and convoluted nature of the 2D multiwavelet and scaling bases.

Acknowledgements

The authors acknowledge the support of the UK Engineering and Physical Sciences Research Council (through grant EP/K031023/1 and the Pennine Water Group Platform Grant EP/I029346/1) and a German DAAD visiting fellowship (grant ID: A 13 72 005).

References

[1] E.F. Toro, P. García-Navarro, Godunov-type methods for free-surface shallow flows: A review, J. Hydraul. Res. 45 (6) (2007) 736–751.
[2] J. Neal, I. Villanueva, N. Wright, T. Willis, T. Fewtrell, P. Bates, How much physical complexity is needed to model flood inundation? Hydrol. Process. 26 (15) (2012) 2264–2282.
[3] S. Néelz, G. Pender, Benchmarking the Latest Generation of 2D Hydraulic Modelling Packages, UK Environment Agency Science Report: SC120002, 2013.
[4] N. Hunter, et al., Benchmarking 2D hydraulic models for urban flooding, Proc. ICE Water Manag. 161 (1) (2008) 13–30.
[5] S. Godunov, A difference method for numerical calculation of discontinuous solutions of the equations of hydrodynamics, Mat. Sb. 89 (3) (1959) 271–306.
[6] P. Brufau, P. García-Navarro, M.E. Vázquez-Cendón, Zero mass error using unsteady wetting–drying conditions in shallow flows over dry irregular topography, Internat. J. Numer. Methods Fluids 45 (10) (2004) 1047–1082.
[7] B.F. Sanders, Integration of a shallow water model with a local time step, J. Hydraul. Res. 46 (4) (2008) 466–475.
[8] M. Morales-Hernández, M.E. Hubbard, P. García-Navarro, A 2D extension of a Large Time Step explicit scheme () for unsteady problems with wet/dry boundaries, J. Comput. Phys. 263 (0) (2014) 303–327.
[9] J.E. Schubert, B.F. Sanders, Building treatments for urban flood inundation models and implications for predictive skill and modeling efficiency, Adv. Water Resour. 41 (0) (2012) 49–64.
[10] M.J. Castro Díaz, J.A. López-García, C. Parés, High order exactly well-balanced numerical methods for shallow water systems, J. Comput. Phys. 246 (0) (2013) 242–264.
[11] V. Caselles, R. Donat, G. Haro, Flux-gradient and source-term balancing for certain high resolution shock-capturing schemes, Comput. & Fluids 38 (1) (2009) 16–36.
[12] E. Audusse, M.-O. Bristeau, A well-balanced positivity preserving second-order scheme for shallow water flows on unstructured meshes, J. Comput. Phys. 206 (1) (2005) 311–333.
[13] M. Dumbser, M. Castro, C. Parés, E.F. Toro, ADER schemes on unstructured meshes for nonconservative hyperbolic systems: Applications to geophysical flows, Comput. & Fluids 38 (9) (2009) 1731–1748.
[14] S. Noelle, Y. Xing, C.-W. Shu, High-order well-balanced finite volume WENO schemes for shallow water equation with moving water, J. Comput. Phys. 226 (1) (2007) 29–58.
[15] G. Vignoli, V.A. Titarev, E.F. Toro, ADER schemes for the shallow water equations in channel with irregular bottom elevation, J. Comput. Phys. 227 (4) (2008) 2463–2480.
[16] V. Caleffi, A. Valiani, A. Bernini, Fourth-order balanced source term treatment in central WENO schemes for shallow water equations, J. Comput. Phys. 218 (1) (2006) 228–245.
[17] J. Hou, Q. Liang, F. Simons, R. Hinkelmann, A stable 2D unstructured shallow flow model for simulations of wetting and drying over rough terrains, Comput. & Fluids 82 (0) (2013) 132–147.
[18] S. Ito, K. Goto, K. Ono, Automatically optimized core mapping to subdomains of domain decomposition method on multicore parallel environments, Comput. & Fluids 80 (0) (2013) 88–93.
[19] J. Lhomme, J. Gutierrez-Andres, A. Weisgerber, M. Davison, J. Mulet-Marti, A. Cooper, B. Gouldby, Testing a new two-dimensional flood modelling system: analytical tests and application to a flood event, J. Flood Risk Manag. 3 (1) (2010) 33–51.

[20] J.E. Schubert, B.F. Sanders, M.J. Smith, N.G. Wright, Unstructured mesh generation and landcover-based resistance for hydrodynamic modeling of urban flooding, Adv. Water Resour. 31 (12) (2008) 1603–1621.
[21] Y. Xing, X. Zhang, C.W. Shu, Positivity-preserving high order well-balanced discontinuous Galerkin methods for the shallow water equations, Adv. Water Resour. 33 (12) (2010) 1476–1493.
[22] J.-F. Remacle, S.S. Frazão, X. Li, M.S. Shephard, An adaptive discretization of shallow-water equations based on discontinuous Galerkin methods, Internat. J. Numer. Methods Fluids 52 (8) (2006) 903–923.
[23] Q. Araud, P. Finaud-Guyot, V. Guinot, R. Mosé, J. Vazquez, An eigenvector-based linear reconstruction approach for time stepping in discontinuous Galerkin scheme used to solve shallow water equations, Internat. J. Numer. Methods Fluids 70 (12) (2012) 1590–1604.
[24] E.J. Kubatko, J.J. Westerink, C. Dawson, hp Discontinuous Galerkin methods for advection dominated problems in shallow water flow, Comput. Methods Appl. Mech. Engrg. 196 (1–3) (2006) 437–451.
[25] C. Dawson, C.J. Trahan, E.J. Kubatko, J.J. Westerink, A parallel local timestepping Runge–Kutta discontinuous Galerkin method with applications to coastal ocean modeling, Comput. Methods Appl. Mech. Engrg. 259 (0) (2013) 154–165.
[26] G. Kesserwani, Q. Liang, A conservative high-order discontinuous Galerkin method for the shallow water equations with arbitrary topography, Int. J. Numer. Methods Eng. 86 (1) (2011) 47–69.
[27] P.A. Tassi, O. Bokhove, C.A. Vionnet, Space discontinuous Galerkin method for shallow water flows—kinetic and HLLC flux, and potential vorticity generation, Adv. Water Resour. 30 (4) (2007) 998–1015.
[28] T. Zhou, Y. Li, C.W. Shu, Numerical comparison of WENO finite volume and Runge–Kutta discontinuous Galerkin methods, J. Sci. Comput. 16 (2) (2001) 145–171.
[29] G. Kesserwani, Topography discretization techniques for Godunov-type shallow water numerical models: a comparative study, J. Hydraul. Res. 51 (4) (2013) 351–367.
[30] G. Kesserwani, Q. Liang, Dynamically adaptive grid based discontinuous Galerkin shallow water model, Adv. Water Resour. 37 (2012) 23–39.
[31] F. Zhou, G. Chen, Y. Huang, J.Z. Yang, H. Feng, An adaptive moving finite volume scheme for modeling flood inundation over dry and complex topography, Water Resour. Res. 49 (4) (2013) 1914–1928.
[32] J. Wackers, G. Deng, A. Leroyer, P. Queutey, M. Visonneau, Adaptive grid refinement for hydrodynamic flows, Comput. & Fluids 55 (0) (2012) 85–100.
[33] M. Nemec, M. Aftosmis, Adjoint error estimation and adaptive refinement for embedded-boundary Cartesian meshes, in: 18th AIAA CFD Conference, Miami, 2007.
[34] B. Alpert, G. Beylkin, D. Gines, L. Vozovoi, Adaptive solution of partial differential equations in multiwavelet bases, J. Comput. Phys. 182 (1) (2002) 149–190.
[35] A. Shelton, Multi-Resolution Discontinuous Galerkin Method for Unsteady Compressible Flows (Ph.D. Thesis), Georgia Institute of Technology, 2008.
[36] R. Archibald, K.J. Evans, J. Drake, J.B. White, Multiwavelet discontinuous Galerkin-accelerated exact linear part (ELP) method for the shallow-water equations on the cubed sphere, Mon. Weather Rev. 139 (2) (2011) 457–473.
[37] N. Hovhannisyan, S. Müller, R. Schäfer, Adaptive multiresolution discontinuous Galerkin schemes for conservation laws, Math. Comp. 83 (285) (2014) 113–151.
[38] N. Gerhard, F. Iacono, G. May, S. Müller, R. Schäfer, A high-order discontinuous Galerkin discretization with multiwavelet-based grid adaptation for compressible flows, J. Sci. Comput. (2014) 1–28.
[39] B. Cockburn, C.-W. Shu, Runge–Kutta discontinuous Galerkin methods for convection-dominated problems, J. Sci. Comput. 16 (3) (2001) 173–261.
[40] F. Keinert, Wavelets and Multiwavelets, Boca Raton, Florida: Chapman and Hall/CRC, 2004.
[41] P.L. Roe, Approximate Riemann solvers, parameter vectors, and difference schemes, J. Comput. Phys. 43 (2) (1981) 357–372.
[42] G. Kesserwani, R. Ghostine, J. Vazquez, A. Ghenaim, R. Mosé, Riemann Solvers with Runge–Kutta discontinuous Galerkin schemes for the 1D shallow water equations, J. Hydraul. Eng. 134 (2) (2008) 243–255.
[43] N. Gerhard, S. Müller, Adaptive multiresolution discontinuous Galerkin schemes for conservation laws: multi-dimensional case, Comp. Appl. Math. (2014) 1–29.